J. Fluid Mech. (2004), *vol.* 502, *pp.* 99–126.
DOI: 10.1017/S0022112003007481 Printed in the United Kingdom

Symmetry breaking in free-surface cylinder flows

By J. M. LOPEZ[1], F. MARQUES[2], A. H. HIRSA[3] AND R. MIRAGHAIE[3]

[1]Department of Mathematics and Statistics, Arizona State University, Tempe, AZ 85287, USA

[2]Departament de Física Aplicada, Universitat Politècnica de Catalunya, Jordi Girona Salgado s/n, Mòdul B4 Campus Nord, 08034 Barcelona, Spain

[3]Department of Mechanical, Aerospace, and Nuclear Engineering, Rensselaer Polytechnic Institute, Troy, NY 12180, USA

(Received 22 April 2003 and in revised form 6 October 2003)

The flow in a stationary open cylinder driven by the constant rotation of the bottom endwall is unstable to three-dimensional perturbations for sufficiently large rotation rates. The bifurcated state takes the form of a rotating wave. Two distinct physical mechanisms responsible for the symmetry breaking are identified, which depend on whether the fluid depth is sufficiently greater or less than the cylinder radius. For deep systems, the rotating wave results from the instability of the near-wall jet that forms as the boundary layer on the rotating bottom endwall is turned into the interior. In this case the three-dimensional perturbations vanish at the air/water interface. On the other hand, for shallow systems, the fluid at radii less than about half the cylinder radius is in solid-body rotation whereas the fluid at larger radii has a strong meridional circulation. The interface between these two regions of flow is unstable to azimuthal disturbances and the resulting rotating wave persists all the way to the air/water interface. The flow dynamics are explored using three-dimensional Navier–Stokes computations and experimental results obtained via digital particle image velocimetry. The use of a flat stress-free model for the air/water interface reproduces the experimental results in the deep system but fails to capture the primary instability in the shallow system, even though the experimental imperfections, i.e. departures from a perfectly flat and clean air/water interface, are about the same for the deep and the shallow systems. The flat stress-free model boundary conditions impose a parity condition on the numerical solutions, and the consideration of an extended problem which reveals this hidden symmetry provides insight into the symmetry-breaking instabilities.

1. Introduction

Flat gas/liquid interfaces are often modelled as stress-free (shear-free) (e.g. Hunt 1984; Pan & Banerjee 1995; Walker, Leighton & Garza-Rios 1996; Handler *et al.* 1999; Teixeira & Belcher 2000), and this idealization is also very common in convection models (e.g. Chandrasekhar 1961; Busse & Bolton 1984; Goldstein *et al.* 1993; Scheel & Seehafer 1997). However, this idealization is never realized physically, even in well-controlled laboratory situations, for a variety of reasons. The free surface is impossible to clean perfectly, and even small amounts of contaminants can impart stress, particularly for air/water interfaces (Davies & Rideal 1963; Scott 1975). As well, the Froude number is not identically zero, so small deformations away from flat are always present. Nevertheless, in many circumstances modelling the free surface

as flat and stress-free is appropriate. One of the central issues to be addressed in this paper is the impact of imperfections on the ideal boundary condition. This is motivated by our attempts to model laboratory experiments with a flat stress-free interface boundary condition. We have been successful in some parameter regimes but not in others, yet in all the parameter regimes the surface was cleaned to the same extent and the Froude number was of the same order, i.e. the level of imperfection was about the same. What we shall demonstrate here is that using a flat stress-free boundary condition implies a hidden symmetry in the problem. The interface in the model is a reflection symmetry plane, so that the computational model has a Z_2 symmetry. The experiments, of course, are not restricted to such an equivariant system because of the imperfections. When the imperfections are small, the basic state is modelled well with the ideal flat stress-free condition. The problem may arise when the basic state becomes unstable, as parameters are varied. If the most unstable mode (in the system without the hidden Z_2 symmetry imposed) is invariant to the Z_2 symmetry, then the ideal condition continues to be appropriate. However, if the bifurcating mode is not Z_2 invariant, then a model with the hidden Z_2 symmetry imposed results in dynamics that are not in accord with those in a system where the hidden symmetry is not imposed (e.g. the physical experiment).

We investigate this problem in a well-controlled laboratory experimental setting, consisting of flow in a stationary circular cylinder, driven by the constant rotation of the bottom endwall, with the upper surface being an essentially flat stress-free air/water interface. As well, we study computational models of the full three-dimensional Navier–Stokes equations in the extended problem consisting of a cylinder of twice the length with both endwalls co-rotating. The mid-plane is a reflection boundary that corresponds to a flat, stress-free interface. Computationally, we study the dynamics in the full problem as well as in various subspaces where certain symmetries are imposed.

This particular flow has previously been studied experimentally, the most comprehensive studies being the PhD thesis of Spohn (1991) and subsequent publications (Spohn & Daube 1991; Spohn, Mory & Hopfinger 1993, 1998). The main focus of those studies was the characterization of the basic state. The experiments used tap water and no attempt was made to reduce the effects of surface-active agents (surfactants). In Spohn & Daube (1991), a simple model to numerically account for surfactant effects was introduced, in response to the observation that the radial velocity at the surface vanished in the experiment, whereas in the stress-free computations this velocity component was non-zero. In Spohn *et al.* (1993) and Spohn *et al.* (1998) it is claimed that since the azimuthal component of the surface velocity was non-zero, surface viscosity effects and azimuthal stresses were negligible. This however says nothing about the radial stresses in their experiment, which were in fact large enough to bring the radial component of velocity to rest. In these axisymmetric flows, surfactants tend to be swept in radially by the surface flow, causing a signifigant radial concentration gradient which leads to a radial gradient in surface tension (i.e. a Marangoni stress) that opposes the radial surface flow. In the azimuthal direction, there is no such stress as the flow is axisymmetric. In a similar flow, Lopez & Hirsa (2000) and Hirsa, Lopez & Miraghaie (2001, 2002*a*) have shown that with insoluble surfactant monolayers, the radial stress can be comparable to that due to a rigid no-slip wall, and yet if the surface shear viscosity of the monolayer system is small, the azimuthal velocity is virtually indistinguishable from that at a stress-free interface.

Hirsa, Lopez & Miraghaie (2002*b*) have performed experiments in a relatively deep cylinder flow driven by a rotating endwall, taking care to have as clean an air/water

interface as possible. Here, we shall compare computations using the ideal stress-free condition with these experiments, and show agreement for the primary instability of the basic state. More extensive experiments were done by Miraghaie (2002), many of which we shall compare with here. For shallow systems however, we find that the model with the ideal stress-free condition fails to capture the primary instability, and we shall show that relaxing the hidden Z_2 symmetry condition provides insight into the problem.

2. Basic equations, symmetries and numerical method

In order to deal explicitly with the hidden Z_2 symmetry imposed by the ideal flat stress-free condition, we shall consider the extended problem of flow in a cylinder of length $2H$ and radius R, driven by the co-rotation of both rigid endwalls at constant angular speed Ω. Using R as the length scale and $1/\Omega$ as the time scale, there are two non-dimensional governing parameters:

$$\text{Reynolds number:} \quad Re = \Omega R^2/\nu,$$
$$\text{aspect ratio:} \quad \Gamma = H/R,$$

where ν is the kinematic viscosity of the fluid.

The equations governing the flow are the Navier–Stokes equations together with initial and boundary conditions. In cylindrical coordinates, (r, θ, z), the non-dimensional velocity vector is $\boldsymbol{u} = (u, v, w)$. The domain is $(r, \theta, z) \in [0, 1] \times [0, 2\pi] \times [-\Gamma, \Gamma]$. The boundary conditions are no-slip for all solid walls and the *essential* pole conditions at the axis (see Lopez, Marques & Shen 2002, for details).

The three-dimensional Navier–Stokes equations are solved numerically using a Galerkin spectral scheme for spatial discretization and a second-order projection scheme for time evolution. Legendre polynomial bases are used in the radial and axial directions and a Fourier basis is used in the periodic azimuthal direction. The details of the numerical method are given in Lopez *et al.* (2002). For the computed results presented here, up to 48 Legendre modes in r, 64 Legendre modes in z, 32 Fourier modes in θ, and a time-step of 2×10^{-2} have been used. The initial condition is either a state of rest or the continuation of a solution from one point in the (Re, Γ)-parameter space to a nearby point in that parameter space.

The governing equations and boundary conditions are equivariant to rotations R_ϕ, of arbitrary angle ϕ, around the cylinder axis, and to a specular reflection K about the mid-plane $z = 0$. Their action on the velocity vector $\boldsymbol{u}$ is

$$R_\phi(u, v, w)(r, \theta, z) = (u, v, w)(r, \theta + \phi, z), \tag{2.1}$$
$$K(u, v, w)(r, \theta, z) = (u, v, -w)(r, \theta, -z). \tag{2.2}$$

Since R_ϕ and K commute, the symmetry group of the problem is $\mathcal{G} = SO(2) \times Z_2$. The basic state, i.e. the unique solution of the Navier–Stokes equations for small values of Re, is steady and invariant to the group $\mathcal{G}$. The problem with a flat stress-free interface in a cylinder of length H driven by the rotation of the bottom endwall is simply the restriction of the extended problem to a Z_2-invariant subspace. With the spectral method used, this restriction is simply accomplished by setting to zero all the odd Legendre polynomials in the z-basis for u and v and all the even Legendre polynomials in the z-basis for w. This enforces the condition

$$u_z = v_z = w = 0, \tag{2.3}$$

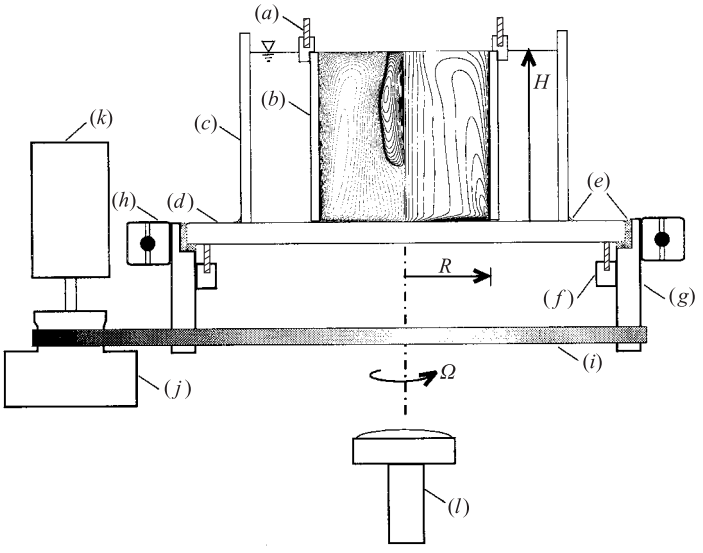

FIGURE 1. Schematic of the flow apparatus; computed streamlines (left meridional half-plane) and vortex lines (right meridional half-plane) of the steady axisymmetric basic state at $Re = 1900$ and $\Gamma = 2$ are shown inside the cylinder. The letters indicate: (*a*) stationary cylinder retainer ring and alignment screws, (*b*) stationary cylinder, (*c*) water container (cylinder), (*d*) rotating bottom, (*e*) silicone sealant, (*f*) rotating bottom alignment screws, (*g*) rotating bottom retainer and belt pulley, (*h*) ball bearing, (*i*) drive belt, (*j*) motor pulley and flywheel, (*k*) stepper motor, and (*l*) DPIV camera.

at the mid-height plane ($z = 0$), which means that on this plane there is no flow-through (maintaining it flat) and there are no tangential stresses.

We shall consider the dynamics in a number of subspaces: (i) the $SO(2) \times Z_2$-invariant subspace, where all solutions are axisymmetric and reflection symmetric about $z = 0$; (ii) the $SO(2)$-invariant subspace, where all solutions are axisymmetric but the mid-plane ($z = 0$) need not be a symmetry plane; (iii) the Z_2-invariant subspace, where the mid-plane ($z = 0$) is a symmetry plane but the solutions need not be axisymmetric; and finally (iv) the full problem where no symmetry conditions are imposed.

3. Experimental technique

The flow in the stationary cylinder of aspect ratio (depth to radius) Γ with the bottom endwall rotating at Ω rad s^{-1} and a free surface was studied using the apparatus depicted in figure 1. The bottom consisted of optical-quality glass (flat to within ± 0.0025 cm) which was retained by a precision ball bearing. The glass bottom was attached to the ball bearing using a retaining cylinder with a compliant silicone sealant, and three fine-pitch alignment screws were utilized to make the rotation plane true to within ± 0.001 cm (at R). The bearing was press-fitted into a 2.5 cm thick polycarbonate plate, which was mounted on an optical table. Several lead bricks (47 kg total) were attached to the polycarbonate plate to reduce any vibrations. The bottom was rotated via a drive belt and a stepper motor fitted with a 10 cm diameter, 5 cm long brass flywheel. The combination of the drive belt, heavy flywheel, and micro-stepping (approximately 41 000 micro-steps per revolution of the bottom), made the rotation of the bottom relatively free from vibrations.

Two cylinders were made of precision bore glass (Ace Glass, Trubore) with inner diameter of 5.006 ± 0.006 cm. For the experiments with a deep cylinder, the glass cylinder was cut to a height of 5.00 ± 0.01 cm ($\Gamma = 2$), and for experiments with a shallow cylinder it was cut to a height of 0.66 ± 0.03 cm ($\Gamma = 0.26$). The cylinder was lightly press-fitted into a retainer, machined from acrylic, that contacted the cylinder at three points to minimize optical blockage. The retainer was held by three fine-pitch screws onto a cover plate (not shown in the figure), allowing the cylinder to be made perpendicular to the rotating bottom. The gap between the cylinder and the rotating bottom was set to 0.007 ± 0.002 cm.

The reproducibility of the flow measurements using this relatively precise apparatus appeared to depend on three factors: (i) the alignment of the cylinder and the centre of rotation of the glass bottom, (ii) the flatness of the air/water interface, and (iii) the absence of surface-active contaminants. The cylinder was centred to within 0.006 cm of the bottom's centre of rotation, using alignment screws on the cover plate. In order to pin the contact line and achieve a flat free surface, the top rim of the cylinder was coated with a thin paraffin film (from a dilute solution in hexane). Thus, by filling the system up to the rim, a flat interface (to within ± 0.005 cm) could be obtained. The paraffin coating of the glass rim did not contaminate the water in the system. The water in the system was contained by a glass cylinder (nominal inner diameter of 11.1 cm, wall thickness of 0.3 cm, cut to a height 0.6 cm larger than the stationary cylinder) with its grounded bottom cemented from the outside to the rotating bottom. The system was filled with double-distilled water (at $22 \pm 0.5\,^{\circ}$C, where the kinematic viscosity $\nu = 0.00957\,\mathrm{cm^2\,s^{-1}}$), and seeded with 21 micron polystyrene particles (Duke Scientific, 7520A) for the digital particle image velocimetry (DPIV) measurements. The procedure described in Hirsa *et al.* (2001) was followed for cleaning the particles. The details of the DPIV system can also be found in Hirsa *et al.* (2001). The purity of the surface of the seeded water was checked by surface tension measurements during rapid compression in a Langmuir trough. The surface was aspirated prior to each experiment in the open cylinder.

4. Base flow

In the absence of imperfections, the system with the ideal flat stress-free boundary is $SO(2)$ invariant, i.e. invariant to arbitrary rotations about the axis, and we have taken much care to minimize imperfections in the experimental apparatus. As such, the basic flow state is axisymmetric and steady. In the extended problem, the basic state is also Z_2 invariant. This means that u and v are even functions of z and that w is an odd function of z. The meridional structure (i.e. in the r- and z-directions) of the basic state, however, is not trivial. It consists of a boundary layer on the rotating bottom disk that is turned into the interior by the stationary cylinder, forming a shear layer that has a jet-like velocity profile in the azimuthal direction. Inside the cylinder in figure 1, the streamlines (left) and vortex lines (right) projected onto the meridional plane for a basic state at $Re = 1900$ and $\Gamma = 2$ are shown; the structure of the shear layer is apparent. The flow has an overturning nature in the meridional plane, as well as a recirculation zone at the axis, as is characteristic of these swirling flows due to centrifugal effects associated with the overturning flow attempting to bring high-angular-momentum fluid in towards the axis. In this example, the meridional flow stagnates on the free surface to form the recirculation. At lower Re, it tends to stagnate on the axis. Detailed accounts of the changes in the structure of the basic state with parameter variation are presented in Spohn *et al.* (1993), Valentine &

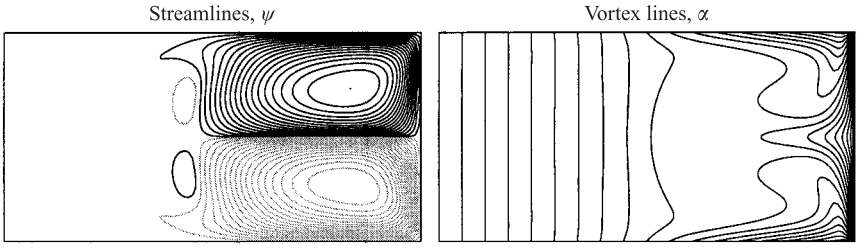

FIGURE 2. Computed basic state at $\Gamma = 0.25$, $Re = 1450$, showing streamlines and vortex lines in a meridional plane $(r, z) \in [0, 1] \times [-\Gamma, \Gamma]$. Contour levels are spaced quadratically; solid (dotted) contours correspond to positive (negative) levels.

Jahnke (1994), Lopez (1995) and Brons, Voigt & Sorensen (2001). Here, we shall show two examples with different aspect ratios Γ that illustrate the primary features that dominate. These features are:

(a) solid-body-rotation of the inner core region, predominately for small Γ;

(b) radial jet of angular momentum at the mid-plane ($z = 0$);

(c) meridional overturning flow in the outer radial part of the flow and the development of an internal jet-like shear layer close to the cylinder wall.

For the base flow, it is often convenient to describe the axisymmetric solutions in terms of the streamfunction, ψ, the axial component of angular momentum, α, and the azimuthal component of the vorticity, η. These are related to the velocity field as

$$\boldsymbol{u} = (u, v, w) = (-\psi_z, \alpha, \psi_r)/r \quad \text{and} \quad \nabla \times \boldsymbol{u} = (-\alpha_z, r\eta, \alpha_r)/r. \tag{4.1}$$

In the same way as contours of ψ give the projection of the streamsurfaces onto a meridional plane (i.e. the streamlines), contours of α give the vortex lines in the meridional plane. For a Z_2-invariant state, ψ is an odd function of z and α is even.

For shallow systems (e.g. $\Gamma = 0.25$, as shown in figure 2), the basic state has some very distinctive features. The streamlines and vortex lines clearly show that for $r < 0.4$ (for this $\Gamma = 0.25$ example), the flow is essentially in solid-body-rotation, with zero meridional motion ($\psi \sim 0$) and the vortex lines aligned with the rotation axis (and $\alpha = rv \propto r^2$, as indicated in the figure where the contour levels are spaced quadratically). In contrast, for $r > 0.4$, there is significant meridional flow as a consequence of the stationary cylinder wall at $r = 1$. The discontinuities between the stationary cylinder and the rotating endwalls result in all of the vortex lines that originate on the rotating walls for $r > 0.6$ terminating at the discontinuities. This results in significant vortex line bending which induces the secondary meridional flow, as indicated by the streamlines. This meridional flow consists of three main features. First, there are the boundary layers on the rotating endwalls for $r > 0.5$, which advect a significant amount of angular momentum out to larger radii. These boundary layers have structure which is described well over most of the disk between about $r = 0.5$ and 1 by the von Kármán similarity solution for boundary layer flow on a rotating disk (Schlichting & Kestin 1979). The stationary cylinder at $r = 1$ turns these endwall layers into the interior, inclined at a small angle away from the cylinder wall, producing the second prominent feature. This second feature is an internal shear layer that has a jet-like profile in the azimuthal direction and strong shear in the meridional direction; we shall refer to this layer as the wall jet-shear layer. Both of these layers (the boundary layers on the endwalls and the wall jet-shear layer) are characteristic of the often studied flow in a cylinder with one stationary endwall and one rotating endwall

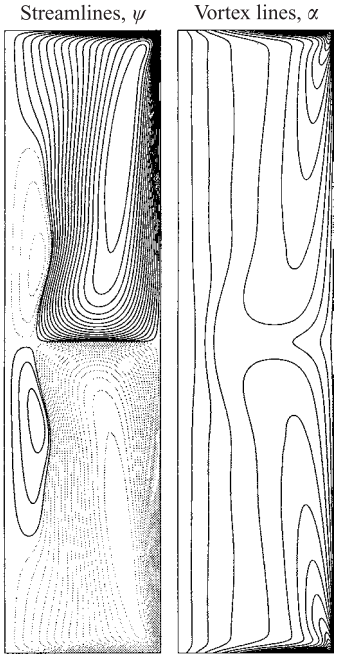

FIGURE 3. Computed basic state at $\Gamma = 2.0$, $Re = 1900$, showing streamlines and vortex lines in a meridional plane $(r, z) \in [0, 1] \times [-\Gamma, \Gamma]$. Contour levels are spaced quadratically; solid (dotted) contours correspond to positive (negative) levels.

(e.g. Escudier 1984; Lopez 1990; Stevens, Lopez & Cantwell 1999; Marques & Lopez 2001; Marques, Lopez & Shen 2002; Blackburn & Lopez 2002). The present problem with two co-rotating endwalls has a third characteristic feature. The boundary layer on the stationary cylinder has flow swirling axially towards the mid-plane ($z = 0$), carrying some angular momentum from both rotating endwalls. At $z = 0$, these two boundary layer flows collide and separate, forming a rather intense internal layer which has jet-like profiles in both the meridional and azimuthal directions. This jet stagnates radially (the azimuthal velocity remains non-zero) as it collides with the region in solid-body-rotation, at about $r = 0.5$. The dynamics associated with a similar internal layer at $z = 0$ have recently been investigated for a related problem, where the flow in the stationary cylinder is driven by the exact counter-rotation of the two endwalls (Nore *et al.* 2003). In that problem, there is no region of solid-body rotation as the fluid in the top half rotates in the opposite sense to that in the bottom half.

On increasing Γ to $\Gamma = 2$ (see figure 3), the region of solid-body rotation near the axis is eliminated. Now, there is meridional circulation (non-zero ψ) throughout the cylinder. The region near the axis is quasi-static, consisting of weak recirculation zones that are either attached to the $z = 0$ plane or to the axis, depending on Re and Γ. These recirculation zones have been visualized experimentally and associated with vortex breakdown bubbles (e.g. Spohn *et al.* 1993). In these deep systems (i.e. large Γ), the wall jet-shear layers are dynamically important and have a structure very similar to those found in stationary cylinder flows of half the length with one stationary endwall and one rotating endwall.

For sufficiently small Re, irrespective of Γ, the basic state is stable. As Re is increased, the basic state loses stability via a variety of Hopf bifurcations, depending on Γ and to which subspace the flow is restricted. The two sample basic states shown

in figures 2 and 3 are at Re values just below critical for each Γ in the full problem (i.e. with no imposed symmetry). In all of the subspaces considered for this problem, the primary bifurcation from the basic state over an extensive range of Γ is found to be of Hopf type. This is also the case in the more widely studied case with one rotating and one stationary endwall, where Gelfgat, Bar-Yoseph & Solan (2001) have shown via three-dimensional stability analysis that for $\Gamma \in [1, 4]$ all bifurcations from the basic state are of Hopf type.

5. Hopf bifurcations from the base flow

Given that the primary instability of the basic state leads to a limit cycle, γ, via a Hopf bifurcation, we now determine what are the possible symmetries of such a limit cycle using group theoretic considerations.

For a generic Hopf bifurcation, a pair of complex-conjugate eigenvalues, $\pm i\omega_0$, cross the imaginary axis as a parameter μ is varied through $\mu = 0$. According to the centre manifold theorem, there exists a two-dimensional centre manifold $\mathscr{M}_c$ and a normal form on it describing the dynamics of the system in a neighbourhood of the bifurcation point (Marsden & McCracken 1976). Using the complex amplitude, A, of the eigenvector corresponding to the eigenvalue $i\omega_0$ to parameterize $\mathscr{M}_c$, the normal form has the form

$$\dot{A} = i\omega_0 A + P(A, \bar{A}, \mu), \tag{5.1}$$

where the polynomial function, P, satisfies

$$P(e^{-i\omega_0 t} A, e^{i\omega_0 t} \bar{A}, \mu) = e^{-i\omega_0 t} P(A, \bar{A}, \mu), \tag{5.2}$$

for all t, from which the standard normal form for the Hopf bifurcation (to third order) is easily derived:

$$\dot{A} = A(i\omega_0 + \mu - a|A|^2). \tag{5.3}$$

The symmetries of the system impose additional conditions on the normal form. If the governing equations are equivariant with respect to $\mathscr{G}$, then so is the normal form. The action of $\mathscr{G}$ on the amplitude A is (see Iooss & Adelmeyer 1998, for details)

$$R_\phi A = e^{im\phi} A, \quad K A = s A, \tag{5.4}$$

where m is an integer and $s = \pm 1$. When $m = 0$, the eigenvector is $SO(2)$-invariant, i.e. axisymmetric; when $s = +1$, the eigenvector is Z_2-invariant.

The additional conditions imposed by the symmetry group $\mathscr{G}$ on P are

$$P(e^{im\phi} A, e^{-im\phi} \bar{A}, \mu) = e^{im\phi} P(A, \bar{A}, \mu), \tag{5.5}$$

$$P(sA, s\bar{A}, \mu) = sP(A, \bar{A}, \mu). \tag{5.6}$$

However, since these conditions can be obtained from (5.2), i.e. letting $t = -m\phi/\omega_0$ gives (5.5), and letting $t = \pi/\omega_0$ gives (5.6) when $s = -1$, there are no additional restrictions on the normal form due to the symmetry group $\mathscr{G} = SO(2) \times Z_2$. The action of $\mathscr{G}$ on the periodic bifurcated solution γ is the following: if $m = 0$, $SO(2)$ leaves every point of γ invariant. If $m \neq 0$, the action of R_ϕ on γ is equivalent to a time translation $t \to t + m\phi/\omega_0$, and γ is a *rotating wave* with precession frequency $\omega_p = \omega_0/m$. If $s = 1$, Z_2 leaves every point of γ invariant. If $s = -1$, the action of the z-flip K is equivalent to a time translation of π/ω_0, which is half the period of γ.

The bifurcated limit cycle γ, as a set, is $\mathscr{G}$-invariant, but the individual points on γ (the solution at a given time), are only invariant to a subgroup Δ of $\mathscr{G}$, called

	m	s	Δ	$\mathcal{G}/\Delta$
I	0	+1	$SO(2) \times Z_2$	**1**
II	0	−1	$SO(2)$	Z_2
III	$\neq 0$	+1	$Z_m \times Z_2$	$SO(2)$
IV	$\neq 0$	−1	Z_{2m}	$SO(2)$

TABLE 1. The symmetries of the bifurcated orbit γ.

the group of *spatial symmetries* of the bifurcated periodic solution. That is, taking a point on γ at a particular time, and applying the symmetry group $\mathcal{G}$, generally does not leave the point invariant, but results in another $\mathcal{G}$-conjugate point on γ. If, instead, the subgroup Δ is applied to the point, the point remains invariant. The remaining elements of $\mathcal{G}$ are called *spatiotemporal symmetries* of γ, and their action is equivalent to a specified time translation along the orbit. The quotient group, $\mathcal{G}/\Delta$, is always either $SO(2)$ or Z_m, except if $\Delta = \mathcal{G}$ and then $\mathcal{G}/\Delta = \mathbf{1}$, the trivial group consisting only of the identity. See Lamb & Melbourne (1999) for a much more general and complete discussion of the symmetries of periodic solutions and their possible bifurcations. Here Z_m, also called C_m, is the cyclic group of m elements.

There are four different possibilities for the symmetries of the bifurcated orbit γ, as shown in table 1, where Z_m is the discrete group of rotations generated by $R_{2\pi/m}$, and Z_{2m} is generated by $KR_{\pi/m}$; the notation $Z_m(R_{2\pi/m})$ and $Z_{2m}(KR_{\pi/m})$ is often used to indicate simultaneously the group and the corresponding generator(s).

In our problem, we have found Hopf bifurcations leading to limit cycles with symmetries corresponding to all four cases. The axisymmetric Hopf bifurcations (types I and II) have been previously studied by restricting the computations to an $SO(2)$-invariant subspace (Valentine & Jahnke 1994; Lopez 1995; Brons *et al.* 2001), but we have found in this present investigation that these take place at Re much larger than the Re at which the basic state undergoes non-axisymmetric Hopf bifurcations (types III and IV). It is on these non-axisymmetric Hopf bifurcations that we focus here.

6. Primary instabilities

6.1. *Deep system:* $\Gamma = 2.0$

6.1.1. *Experimental findings*

Figure 4 shows the axial vorticity and horizontal velocity at a depth $z = -0.24\Gamma$ (i.e. 0.24Γ below the free surface at $z = 0$), measured using DPIV. A horizontal laser light sheet of 0.1 cm (or $0.02H$) thickness was utilized in this measurement. The figure shows that at $Re = 1900$ the flow is essentially axisymmetric. DPIV measurements at various depths (not shown) were taken to verify the axisymmetry of the flow. The recirculation zone in the centre (see the computed streamlines in the meridional plane shown in figure 3) is delineated by the inner radius of the annular region with large axial vorticity (darkest contour level). The boundary layer on the cylinder (negative axial vorticity) is visible in the four corners of the plot. The slightly wavy pattern in some of the vorticity contours in the figure is an inherent characteristic of DPIV measurements of a vortex using a rectangular array and is due to quantization. For $Re > 1900$, the flow becomes non-axisymmetric, with a predominant azimuthal wavenumber $m = 4$.

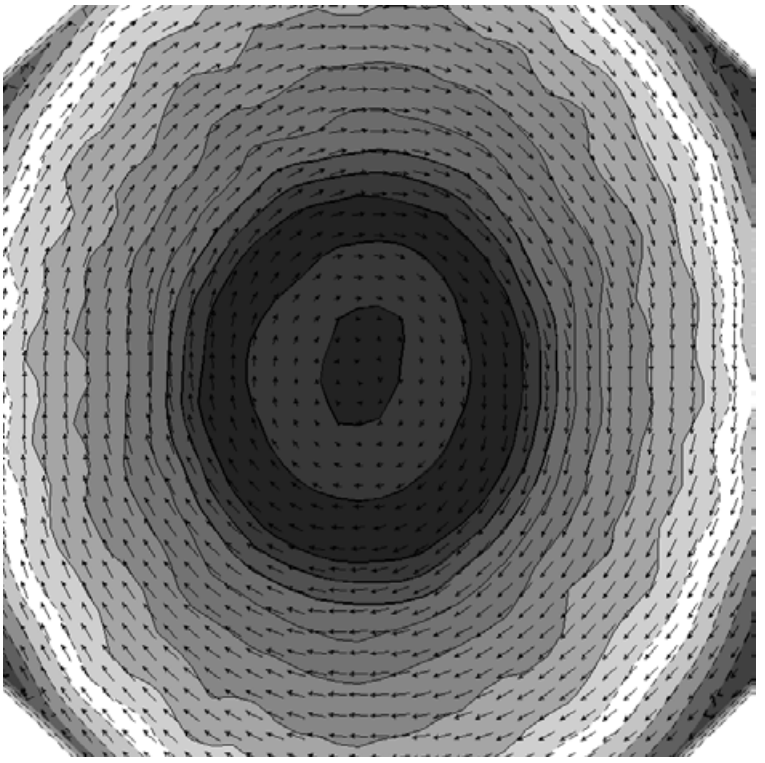

FIGURE 4. Measured axial vorticity (contours) and horizontal velocity (arrows), obtained via DPIV in a deep system with $\Gamma = 2$, at depth $z = -0.24\Gamma$, for a steady axisymmetric basic state at $Re = 1900$.

To explore the nature of the symmetry breaking leading to the rotating wave with azimuthal wavenumber $m = 4$, RW_4, we shall examine how its amplitude varies with Re. As a measure of the amplitude, we use the area integral of the perturbation axial vorticity squared, $\langle \omega_p^2 \rangle$. The perturbation axial vorticity, ω_p, is determined by subtracting the azimuthally averaged axial vorticity from the local axial vorticity, and is non-dimensionalized by Ω. The perturbation axial vorticity measured at a depth $z = -0.24\Gamma$ is shown in figure 5. These data were obtained at $Re = 2200$. A rotating wave with dominant mode $m = 4$ is evident. It should be noted that the positive patches of ω_p (solid line contours) near 5 and 11 o'clock appear stronger than the two positive patches at 2 and 8 o'clock. This is probably due to their proximity to the boundaries of the measurement region and other measurement uncertainties, but could also be indicative of an $m = 2$ component of the flow. The negative patches (broken line contours) of vorticity observed near 1, 4, 7, and 10 o'clock are indicative of a mode $m = 4$ wave. Vorticity determined from DPIV measurements is inherently noisier than velocity measurements and perturbation vorticity is even more difficult to determine accurately. Further complicating the experimental results is the fact that the measurements have to be phase averaged to reduce the noise to an acceptable level, and this phase averaging naturally biases the results. The area integration was performed only up to $r \approx 0.87$ in order to minimize error due to DPIV noise near the wall at $r = 1$. Due to the Cartesian nature of the vorticity DPIV measurements, the data had to be transformed into polar coordinates prior to averaging in the azimuthal direction. The algorithm for transforming the Cartesian data into polar coordinates

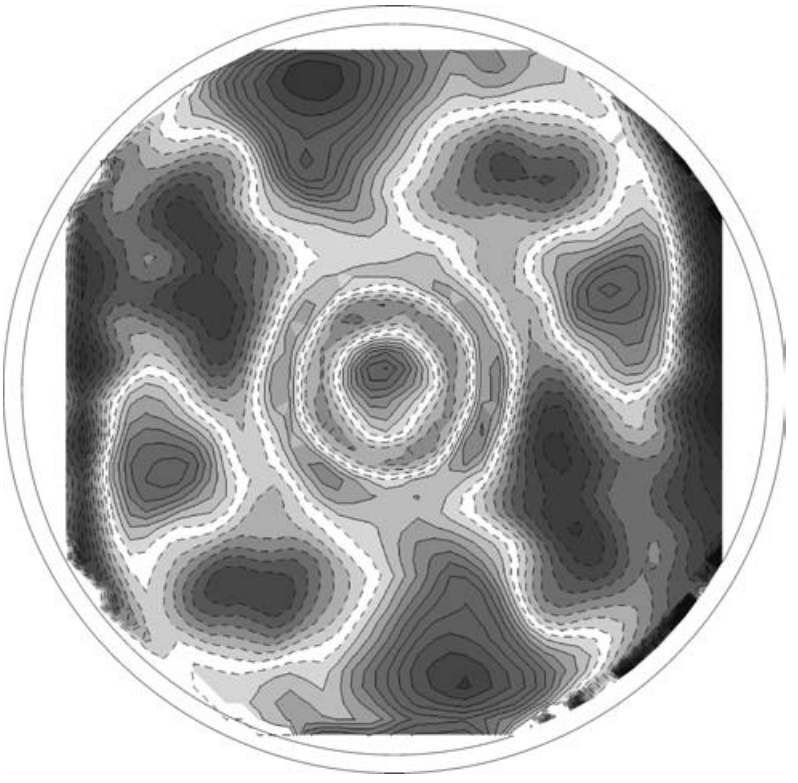

FIGURE 5. Measured perturbation axial vorticity, ω_p, at $Re = 2200$, $\Gamma = 2.0$, at depth $z = -0.24\Gamma$. The DPIV data are phase-averaged over $\pi/2$ in θ.

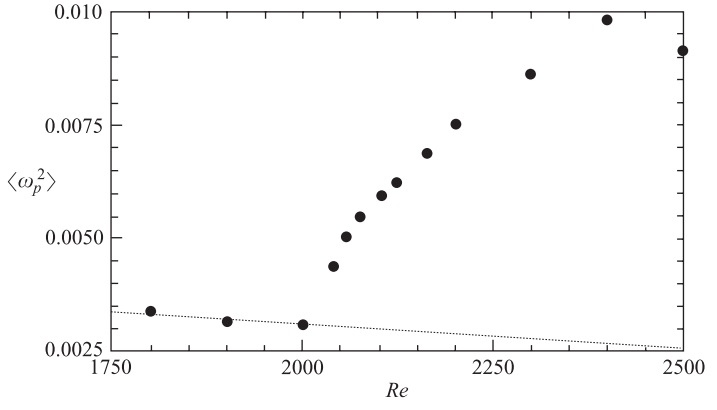

FIGURE 6. Variation of measured $\langle \omega_p^2 \rangle$ with Re for $\Gamma = 2.0$. The dotted line represents the baseline noise level in the DPIV measurements.

involved a single parameter, N, giving the number of points in the Cartesian data set that are interpolated into a discrete annular grid (details are provided in Miraghaie 2002).

Figure 6 shows the variation of the squared perturbation axial vorticity, averaged over the disk $(r, \theta) \in [0, 0.87) \times (0, 2\pi]$ at depth $z = -0.24\Gamma$, $\langle \omega_p^2 \rangle$, with Re. The dotted line in the figure represents the base DPIV noise level. For $Re > 2000$, $\langle \omega_p^2 \rangle$ clearly

rises above the DPIV noise in an almost linear fashion, indicative of a supercritical Hopf bifurcation. The precession of the $m=4$ structure does not vary much with Re, and is finite at onset (Hirsa *et al.* 2002*b*). The data shown in the figure used $N=36$ to determine $\langle\omega_p^2\rangle$. We have found that varying N from 4 to 64 changes $\langle\omega_p^2\rangle$ by less than $\pm 10\%$. However, the extrapolated value of Re for the supercritical Hopf bifurcation (approximately 2000) was found to be independent of N for the range of values considered.

The structure of the dominant mode ($m=4$) observed in the experiments at $Re=2500$ is shown in figure 7, consisting of contours of axial vorticity, solid (broken) lines representing positive (negative) values and the darkest shade representing the extremums, together with vectors representing the projection of the velocity onto the horizontal planes at depth z as indicated. The data were obtained by phase-averaging the DPIV measurements at each 1/4 rotation of the wave over a period of 100 s in order to reduce the random DPIV noise. Note, the extent of the measurement region for depths $z=0$ and $z=-0.08\Gamma$ was reduced due to blockage of the laser light sheet by the cylinder retaining tabs (see figure 1). The flow in the inner region remains essentially axisymmetric, although there is a hint of an $m=2$ component at depth $z=-0.16\Gamma$ for small r. The data show that the $m=4$ rotating wave is strongest at a small distance below the free surface ($z\in[-0.16\Gamma,-0.40\Gamma]$) and at $r\sim 0.7$, indicating that the instability is of the jet-shear layer that is produced as the shear layer that forms on the rotating bottom is turned into the interior by the stationary cylinder (see the description of this for the basic state in §4). This same physical mechanism breaking the $SO(2)$ symmetry of the jet-shear layer has been identified in three-dimensional computations for the case of a stationary rigid top (Marques & Lopez 2001; Blackburn & Lopez 2002).

All of the data points for $Re>2000$ shown in figure 6 are for cases that we have identified as having dominant mode $m=4$ for this geometry ($\Gamma=2.0$). However, occasionally, in some experiments we have observed other rotating wave states, namely modes $m=3$ and $m=5$, as shown in figure 8. These are transient states (eventually an $m=4$ state is established) and their occurrence appears to depend on departures from a flat free surface, surface contamination, and initial flow conditions.

The profiles of radial and azimuthal velocity measured at the free surface ($z=0$) are presented in figure 9 for $Re=2500$ and $\Gamma=2$. These data were obtained via DPIV and were averaged in time. The finite radial velocity for $r>0.2$ (directed in towards $r=0$) confirms that the surface is essentially clean; contaminants would have been swept in towards $r=0$, setting up a concentration gradient and hence a surface tension gradient leading to a Marangoni stress that would have stagnated the radial flow (Lopez & Hirsa 2000; Hirsa *et al.* 2001).

6.1.2. *Numerical results*

Previous axisymmetric computations (Lopez 1995; Brons *et al.* 2001) have determined that the basic state undergoes a supercritical axisymmetric Hopf bifurcation at $Re>2500$, i.e. at much larger Re than that for the symmetry-breaking Hopf bifurcation to a rotating wave we have observed experimentally. We have repeated the computations here, restricted to an $SO(2)\times Z_2$ subspace, and have found that this Hopf bifurcation occurs at $Re\approx 2660$ for $\Gamma=2$; the symmetry of the bifurcated state corresponds to type I in the classification given in table 1. Our experimental observations (and computations not restricted to symmetric subspaces, detailed below) are consistent with the flow visualization experiments of Spohn *et al.* (1998) which report instability at $Re\sim 2000$, but they do not detail the nature of

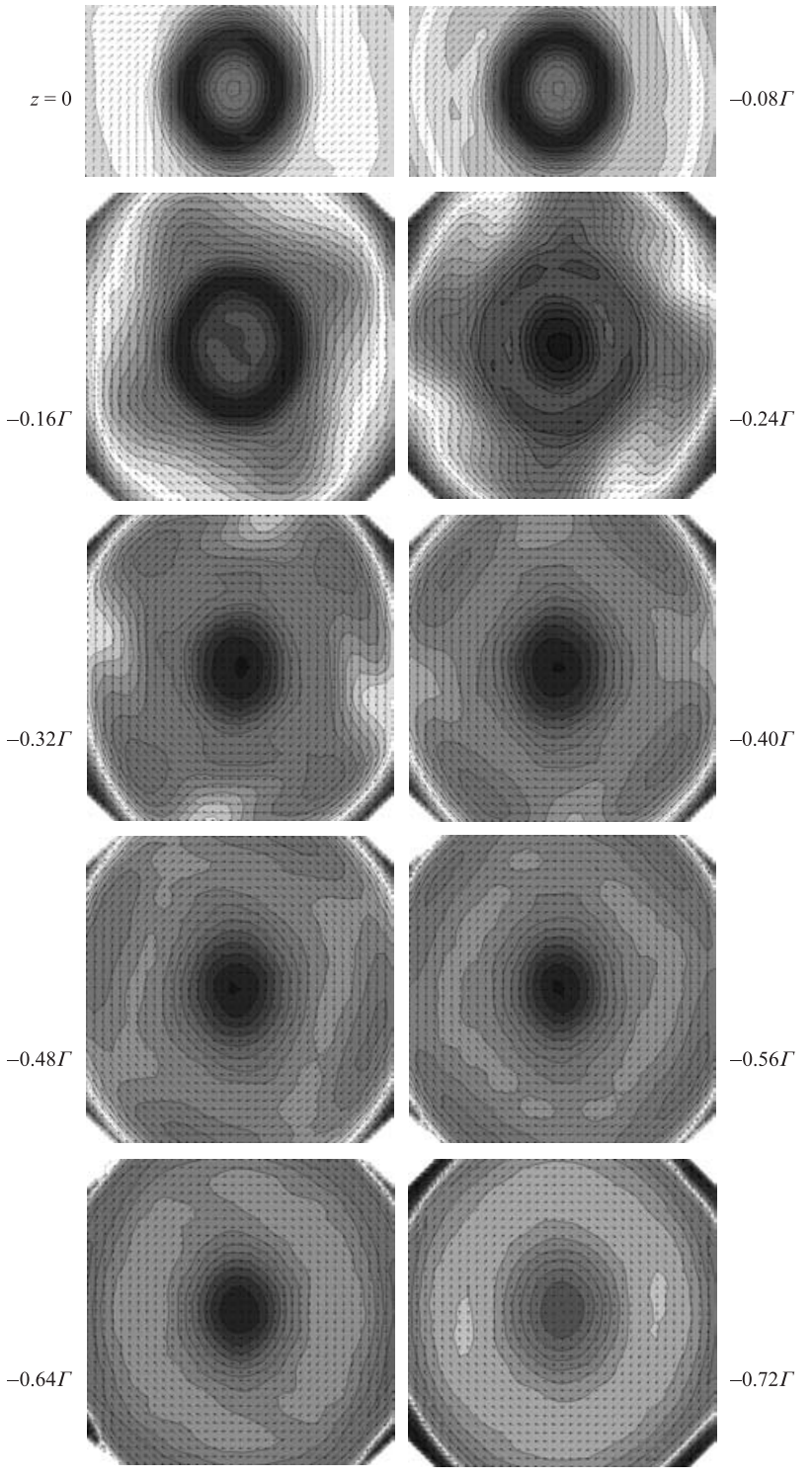

FIGURE 7. Measured axial vorticity (contours) and horizontal velocity (arrows), in a deep system with $\Gamma = 2$ and $Re = 2500$, at depth z below the free surface as indicated.

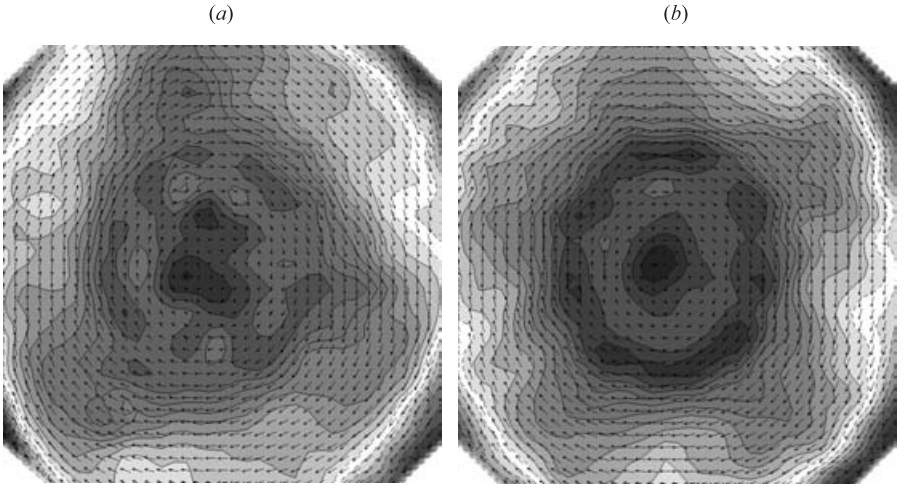

FIGURE 8. Experimentally observed transient states with (*a*) $m=3$ and (*b*) $m=5$ azimuthal wavenumbers. These contours of axial vorticity and projected velocity vectors were measured at depth $z=-0.24\Gamma$ in separate experimental runs with $Re=2200$ and $\Gamma=2$.

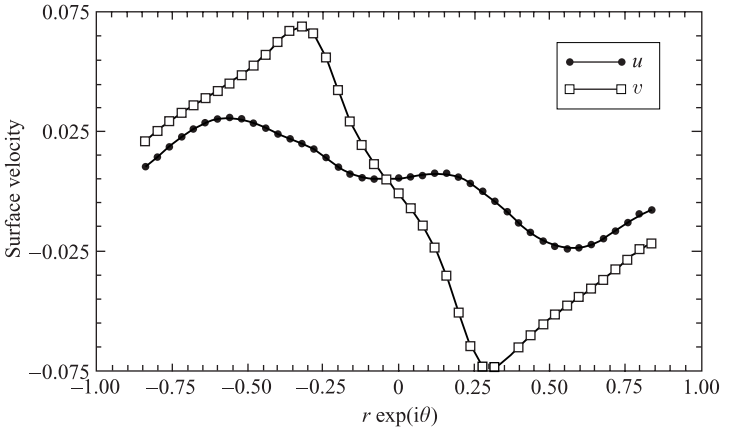

FIGURE 9. Measured profiles of the radial and azimuthal velocity, u and v, at the free surface ($z=0$) across the diameter of the surface nominally going through the origin, $r=0$; the right half of the plot is at an azimuthal angle $\theta=0$ and the left half at angle $\theta=\pi$. The velocities are non-dimensionalized by ΩR. These correspond to an $m=4$ mode at $Re=2500$ and $\Gamma=2$, but time-averaging is essentially equivalent to averaging in θ.

the instability nor its physical origin. From our DPIV measurements of the velocity and corresponding vorticity, it is apparent that the symmetry breaking is due to an azimuthal instability of the shear layer that is produced by the turning of the boundary layer on the rotating disk into the interior, and that the central recirculation zone plays no role in this instability. This is the same physical mechanism identified in long cylinders ($H/R>2$) with a no-slip stationary top (Marques & Lopez 2001; Blackburn & Lopez 2002).

For the deep system with $\Gamma=2$, our numerical computations of the full problem (i.e. no imposed restrictions to symmetric subspaces) show very similar dynamics to the experiments for the primary instability. The basic state remains stable up to about

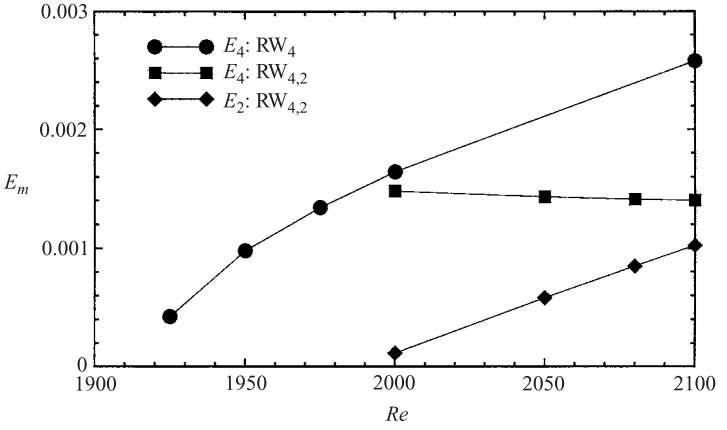

FIGURE 10. Variation with Re of E_4 for RW_4, and E_4 and E_2 for $RW_{4,2}$, computed for $\Gamma = 2$.

$Re = 1910$, at which point it loses stability via a supercritical Hopf bifurcation to an azimuthal mode with wavenumber $m = 4$. This mode is a rotating wave, RW_4. The symmetry of this state corresponds to type III in the classification in table 1, with $m = 4$, $s = +1$, $\Delta = Z_4 \times Z_2$ and $\mathscr{G}/\Delta = SO(2)$. We can monitor its amplitude by the modal energy contained in wavenumber $m = 4$. The modal energies are defined to be

$$E_m = \frac{1}{2} \int_{z=-\Gamma}^{z=\Gamma} \int_{\theta=0}^{\theta=2\pi} \int_{r=0}^{r=1} \boldsymbol{u}_m \cdot \bar{\boldsymbol{u}}_m \, r \, \mathrm{d}r \, \mathrm{d}\theta \, \mathrm{d}z, \tag{6.1}$$

where $\boldsymbol{u}_m$ is the mth Fourier mode of the velocity field. Since the spatial structure of a rotating wave is invariant in a rotating frame (i.e. precessing with the wave), the modal energies are time-independent once the rotating wave state is established. Figure 10 shows E_4 for RW_4 for various values of Re; the supercritical nature of the Hopf bifurcation is evident from the linear growth of E_4 from zero at about $Re = 1910$.

The spatial structure of the Hopf mode leading to RW_4 is shown in figure 11. The figure shows isosurfaces of the $m = 4$ Fourier components of the velocity, at levels ± 0.003 for all three components (this is roughly half of the extreme values); the light (dark) grey isosurfaces are positive (negative). It is clear that $u_4(r, \theta, z) = u_4(r, \theta, -z)$, $v_4(r, \theta, z) = v_4(r, \theta, -z)$, and $w_4(r, \theta, z) = -w_4(r, \theta, -z)$, so this Hopf mode is reflection symmetric (Z_2) about $z = 0$, i.e. has even parity in z with $s = +1$.

In figure 12 contours at various depths of the computed axial vorticity for RW_4 at $Re = 1950$ are shown. These should be compared with the experimentally determined axial vorticity in figure 7 for the $m = 4$ state at $Re = 2500$. Even though there is a considerable difference in Re between them, the distribution of angular momentum for the two cases is remarkably similar, indicating that they are essentially the same state. We say essentially because as we increase Re in the computations, RW_4 becomes unstable, yet the underlying $m = 4$ component of the flow remains predominant.

At about $Re = 1990$, the rotating wave becomes unstable to an $m = 2$ azimuthal mode (see the linear growth of E_2 for $Re > 1990$ at the expense of E_4 in figure 10). This instability of the rotating wave RW_4 is via a period-doubling bifurcation (rather than a Neimark–Sacker bifurcation). If it were a Neimark–Sacker bifurcation, the $m = 4$ and $m = 2$ components would have incommensurate 'precession frequencies' and the resultant state would have been a modulated rotating wave whose structure is not time-invariant in any rotating frame. The structure would have been time-periodic

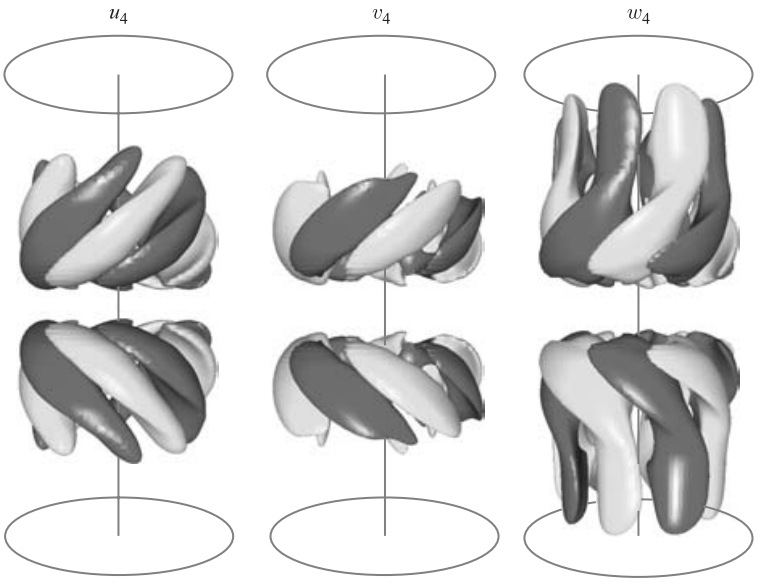

FIGURE 11. Computed isosurfaces of the $m=4$ velocity components of RW_4 at $Re=1950$, $\Gamma=2.0$ with even z-parity; isolevels at ± 0.003.

in a frame rotating at one of the two 'precession frequencies' and the modal energies would also be time-periodic. With a period-doubling bifurcation, the structure is time-invariant in a rotating frame and the modal energies are also time-independent. The precession frequency remains the same, and the symmetry of the period-doubled rotating wave, $RW_{4,2}$, is still type III but with $m=2$, $s=+1$, $\Delta=Z_2\times Z_2$ and $\mathscr{G}/\Delta=SO(2)$.

Period doublings have previously been reported in an experiment with a free surface and $\Gamma=2$ by Young, Sheen & Hwu (1995). They obtained temporal spectra using a single-point laser-Doppler velocimeter system, although they did not report on the spatial structure of the instabilities. For $Re<1900$, they report only steady flow (the basic state), then for $Re=1900$ and 2100 the spectra show a single frequency peak. For $Re=2200$ and 2300 the spectra has a peak at about the same frequency as in the lower-Re cases plus another peak at about half that frequency. At higher Re they observe another period doubling and then more complicated spectra. The Re values for the first onset of time-periodic flow and then for the first period doubling are consistent with our computed results.

Figure 13 shows that the growth rate of E_2 is very slow near the period-doubling bifurcation, and this allows us to compute the unstable RW_4 state for $Re>1990$. In fact, when one starts a computation from rest with $Re\geqslant 2000$ (RW_4 unstable), an RW_4 state is first established which, due to instability, has E_2 growing from very small initial values until it saturates and then the state evolves to $RW_{4,2}$. Figure 13 shows the temporal evolution of E_2 and E_4 for $Re=2000$ (near onset of $RW_{4,2}$) and $Re=2100$ (at this higher Re, $RW_{4,2}$ is itself unstable, see below). For $Re=2000$, $RW_{4,2}$ is not established until about 2×10^4 time units following the initiation of the flow; in the physical experiment this corresponds to about 6000 s. For $Re=2100$, the growth rate of E_2 is much larger and $RW_{4,2}$ is established by about $t=5000$ (about 1500 s). The $Re=2100$ case shown was computed in a Z_2-subspace; at about

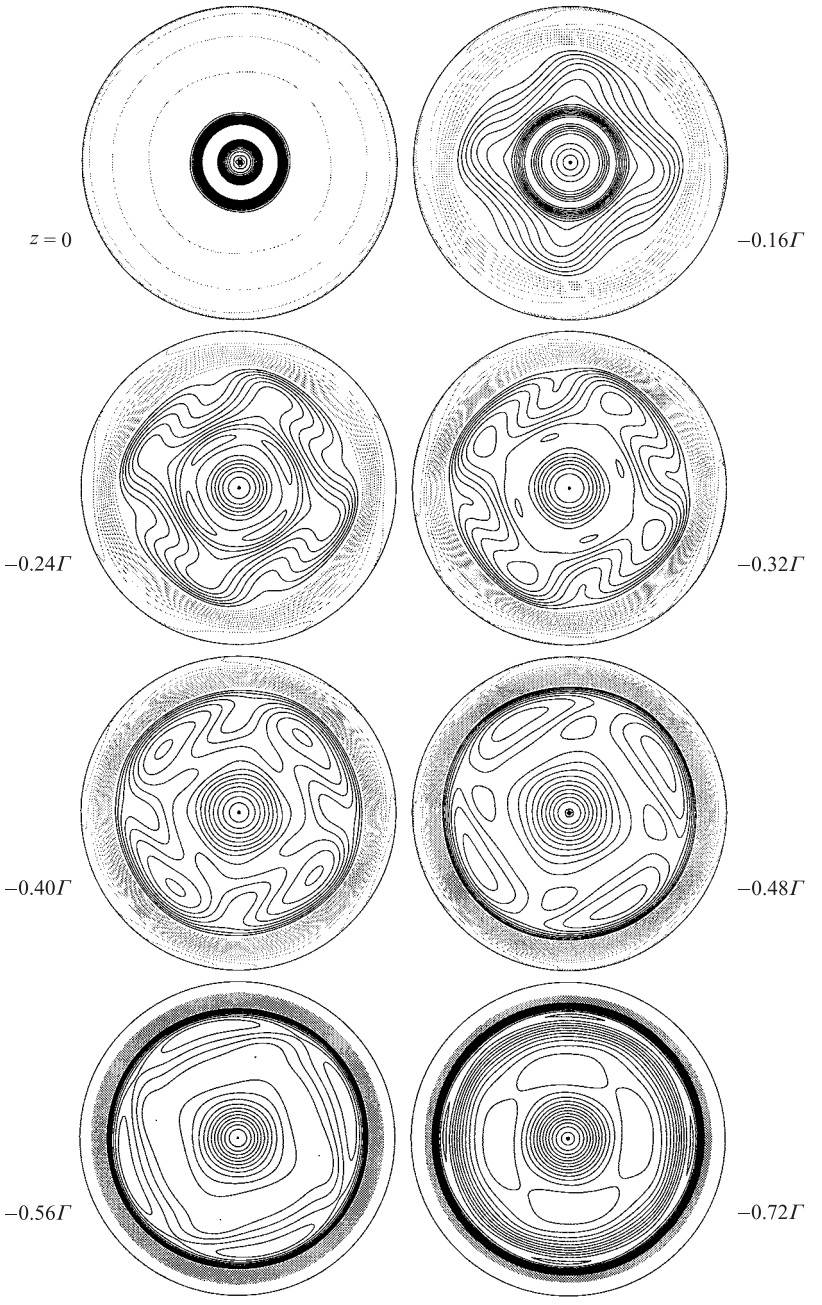

FIGURE 12. Computed axial vorticity of RW_4 at $\Gamma = 2$ and $Re = 1950$, at z as indicated ($z = 0$ is the mid-plane).

$Re = 2085$, the Z_2 symmetric $RW_{4,2}$ becomes unstable to an $m = 3$ mode that breaks the Z_2 reflection symmetry about $z = 0$.

The sequence of bifurcations just described over the range $Re \in [1900, 2100]$ is rather complicated and their effect on the solution state is subtle and difficult to discern. To illustrate this, we plot in figure 14 contours of the radial velocity, u,

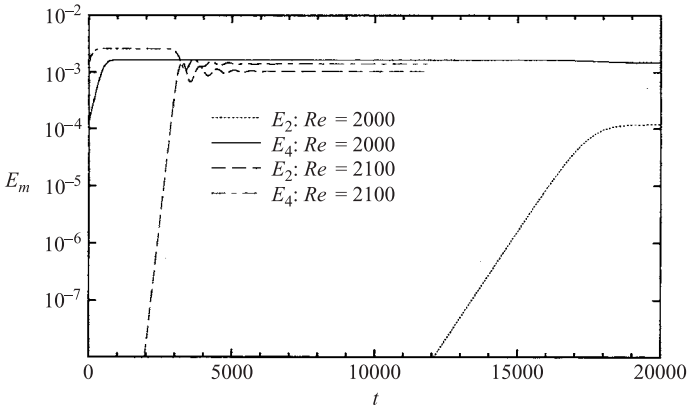

FIGURE 13. Evolution of E_2 and E_4 following a start from rest computed for $\Gamma = 2$ and $Re = 2000$ and 2100.

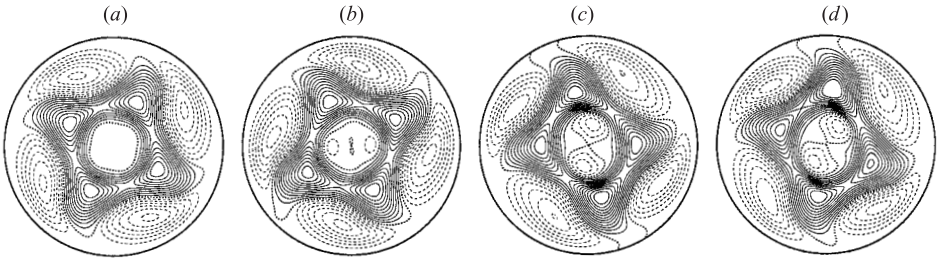

FIGURE 14. Computed radial velocity, u, at depth $z = -0.25\Gamma$, $\Gamma = 2$, for (a) RW_4 at $Re = 1975$, (b) $RW_{4,2}$ at $Re = 2000$, (c) $RW_{4,2}$ at $Re = 2100$, and (d) $MRW_{2,3}$ at $Re = 2100$. The contour levels are uniformly spaced in the interval $u \in [-0.025, 0.025]$, with 12 positive (solid lines) and 12 negative (dotted lines) contours, and the zero contour is dashed.

at depth $z = -0.25\Gamma$ for a number of Re: (a) RW_4 at $Re = 1975$, (b) $RW_{4,2}$ at $Re = 2000$, (c) $RW_{4,2}$ at $Re = 2100$, and (d) $MRW_{2,3}$ at $Re = 2100$. Comparing (a) and (b), we see that the period doubling comes about by the central core region developing an $m = 2$ component which slightly modifies the $m = 4$ outer structure. In (c), the $m = 2$ component has become significantly more energetic (see energy levels in figure 10), but the $m = 4$ outer structure is still predominant. Even in (d), where the $RW_{4,2}$ has become unstable to an $m = 3$ component leading to a modulated rotating wave, $MRW_{2,3}$, that is not invariant to any azimuthal rotation, the underlying $m = 4$ component is clearly predominant. The structure 'precesses' at about the same rate as in (a), but both the structure and the precession are modulated in time. The level of distortion to RW_4 caused by the period-doubling bifurcation and then by the Neimark–Sacker bifurcation introducing the $m = 3$ component is relatively small, and so these states in a physical system would be practically indistinguishable from a RW_4 using either flow visualization or quantitative measurements, such as DPIV with a typical signal-to-noise ratio of order 10^2.

The state shown in figure 14(d) is a modulated rotating wave, $MRW_{2,3}$. The $RW_{4,2}$ becomes unstable at about $Re = 2085$ to an $m = 3$ mode. The symmetry of the $m = 3$ mode (not of the whole solution, $MRW_{2,3}$, but of the Floquet mode) is of type IV with $m = 3$, $s = -1$, $\Delta = Z_6$ and $\mathscr{G}/\Delta = SO(2)$. The most significant point is that this mode breaks the Z_2 reflection symmetry about $z = 0$. The onset of this mode is via

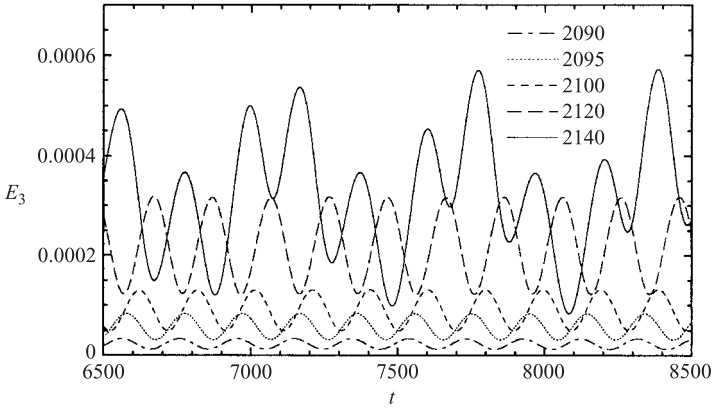

FIGURE 15. Time series of E_3 for $\mathrm{MRW}_{2,3}$ states computed for $\Gamma = 2$ and Re as indicated.

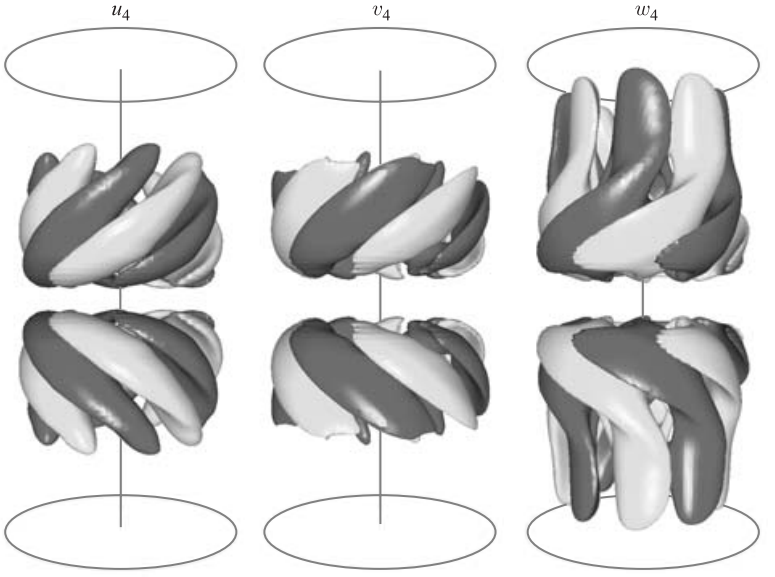

FIGURE 16. Computed isosurfaces of the $m = 4$ velocity components of $\mathrm{MRW}_{2,3}$ at $Re = 2100$, $\Gamma = 2$; isolevels at ± 0.003.

a Neimark–Sacker bifurcation from $\mathrm{RW}_{4,2}$, and so the modal energies are now time-periodic. In figure 15, time series of E_3 for $\mathrm{MRW}_{2,3}$ are shown for various Re. For Re from onset (at about 2090), up to about $Re = 2120$, E_3 is harmonic with a mean that grows approximately linearly with Re. By $Re = 2140$, the exchange of energy between the various components of the flow becomes rather more complicated.

To investigate the structure of the $\mathrm{MRW}_{2,3}$ state at $Re = 2100$, isosurfaces of the radial, azimuthal and axial components of the $m = 4$, 2 and 3 Fourier modes of the velocity are plotted in figures 16, 17 and 18, respectively. The other Fourier modes (except the $m = 0$ mode) have essentially no energy for this state. Figure 16, showing the $m = 4$ mode, is very similar to figure 11; there are only minor differences due primarily to the difference in Re (1950 and 2100), even though figure 11 is for RW_4. The $m = 4$ mode in $\mathrm{MRW}_{2,3}$ is due to the same physical instability mechanism that

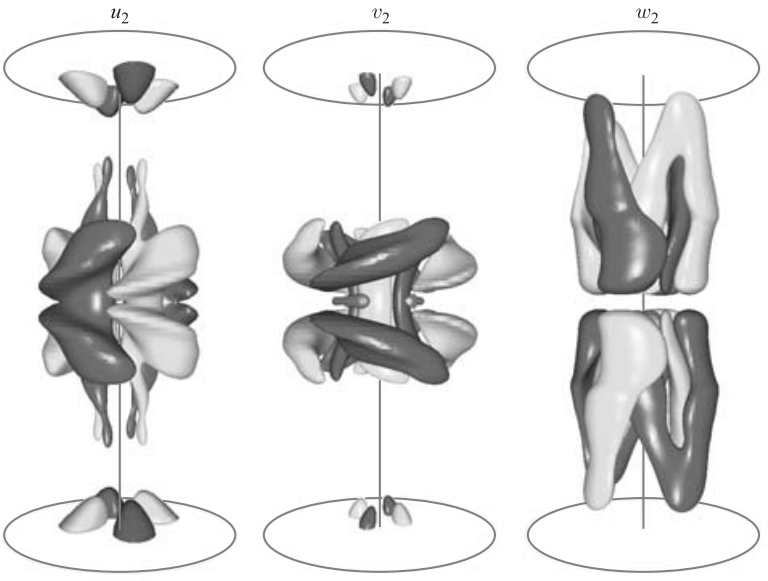

FIGURE 17. Computed isosurfaces of the $m=2$ velocity components of $\mathrm{MRW}_{2,3}$ at $Re=2100$, $\Gamma=2$; isolevels at ± 0.003.

lead to RW_4 described earlier. The $m=2$ mode, shown in figure 17, has the same symmetry type in the axial direction as the $m=4$ modes: they both have even parity in z with $s=+1$. The physical mechanism responsible for the $m=2$ mode, however, is quite different to that for the $m=4$ mode. The isosurfaces show that the $m=2$ mode is closely associated with the recirculation zone attached to $z=0$ near the axis (see figure 3 for an example of the recirculation zone at a lower Re; the structure is not very different at $Re=2100$). An analogous secondary instability of the core region in the flow with a stationary no-slip top at $z=0$ was investigated by Marques & Lopez (2001).

Figure 18 shows the $m=3$ mode. The isosurfaces indicate that the physical mechanism is the same as that responsible for the $m=4$ mode, i.e. instability of the jet-shear layer. However, there is a major difference with the $m=4$ mode in that the $m=3$ mode breaks the Z_2 reflection symmetry about $z=0$; the $m=3$ mode has odd parity in z with $s=-1$. From the figure, it is evident that u_3 and v_3 are odd in z and w_3 is even in z. However, this is a rather degenerate mode in that although w_3 is even in z, w_3 still vanishes at $z=0$ (to within computational noise). This means that although the $m=3$ mode breaks the reflection symmetry about $z=0$, the $z=0$ plane continues to be a plane where the complete axial velocity, w, vanishes and so there is no deformation of this plane. It should be noted that this mode does not exist in a system with stress-free boundary conditions imposed, even though it does not deform the interface; this mode has u_z, v_z different from zero, but still $w=0$ at the interface $z=0$. The stress-free conditions impose a hidden Z_2 symmetry in z which restricts solutions to having even parity in z.

6.2. *Shallow system:* $\Gamma=0.25$

The dynamics in the shallow system are dramatically different to those in the deep system. In particular, the primary mode of instability from the basic state has odd parity in z. This odd parity mode has azimuthal wavenumber $m=3$, and leads to a

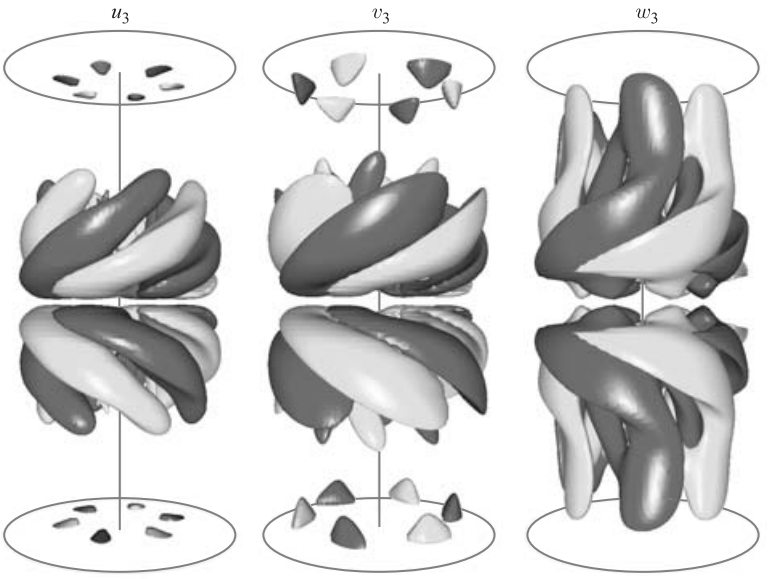

FIGURE 18. Computed isosurfaces of the $m=3$ velocity components of $\mathrm{MRW}_{2,3}$ at $Re=2100$, $\Gamma=2$; isolevels at ± 0.0005.

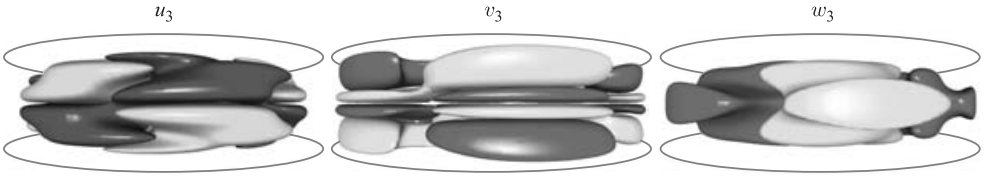

FIGURE 19. Computed isosurfaces of $m=3$ velocity components of RW_3 with odd z-parity at $Re=1500$, $\Gamma=0.25$; isolevels at ± 0.003.

rotating wave RW_3. Figure 19 presents computed isosurfaces of the $m=3$ component of velocity of RW_3, near onset at $Re=1500$, from which the odd z-parity is clearly evident. Notice that in this shallow odd-parity mode, the axial velocity is large at $z=0$. This results in large deformations away from flatness of the $w=0$ isosurface; i.e. the $z=0$ mid-plane is no longer a symmetry plane.

A detailed view of RW_3 and the $m=3$ odd-parity mode is provided in figure 20, where contours of the axial velocity, w, and its $m=3$ Fourier component, w_3, are plotted at various z-levels. From this figure, it is evident that the complete velocity does not have either odd or even z-parity, i.e. $w(r,\theta,z,t) \neq \pm w(r,\theta,-z,t)$, but w_3 does have odd z-parity, i.e. $w_3(r,\theta,z,t)=w_3(r,\theta,-z,t)$. The symmetry of RW_3 is of type IV in the classification in table 1, with $m=3$, $s=-1$ and $\Delta=Z_6(K\,R_{\pi/3})$; w_3 also has this spatial symmetry. In figure 20(a), the complete axial velocity, w, appears to be almost an odd function of z; this is because the basic state w is an odd function of z and we are very close to the Hopf bifurcation, so the amplitude of the Hopf mode is relatively small. However, at $z=0$, where w of the base state is zero, we see that w for RW_3 consists of the corresponding w from the $m=3$ component, which is non-zero due to its odd z-parity (note that the contour levels used in parts a and b differ by an order of magnitude). The figure also indicates that the physical mechanism responsible

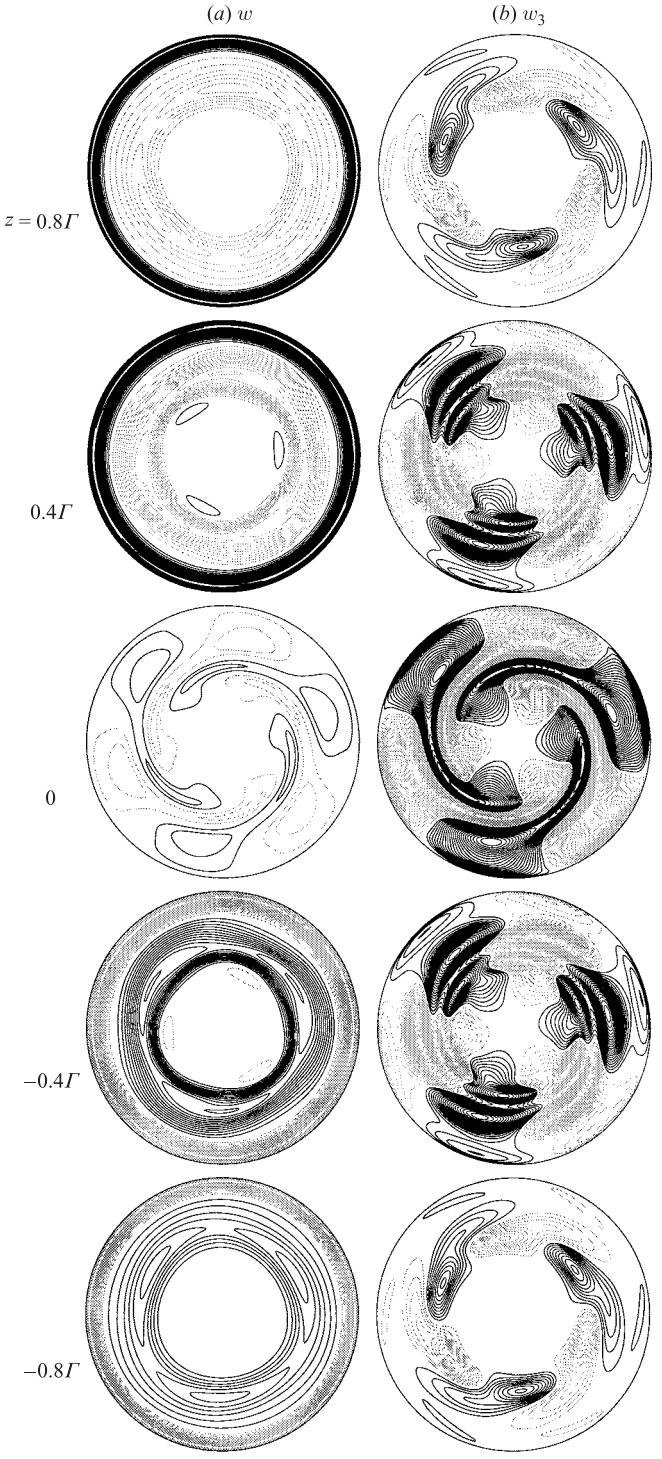

FIGURE 20. Computed axial velocity, w, and its $m=3$ component, w_3, in a shallow system with $\Gamma=0.25$ and $Re=1500$ at depths z as indicated. The range of contour levels for w is ± 0.15, and for w_3 is ± 0.018.

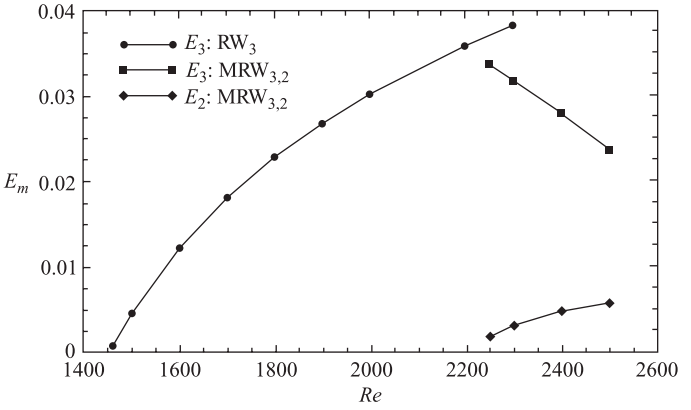

FIGURE 21. Variation with Re of E_3 for RW_3, and E_3 and E_2 for $MRW_{3,2}$, computed for $\Gamma = 0.25$.

for the primary symmetry breaking is different to the instability of the jet-shear layer in the deep system. In this shallow system, the mode has maximum magnitude at mid-depth $z = 0$ and consists of large undulations in (θ, z) from the cylinder wall at $r = 1$ to about mid-radius (see the contours of w_3 at $z = 0$). At mid-radius, $r \approx 0.5$, the large perturbations spread axially in the $\pm z$-directions along the interface between the solid-body rotation in the inner core and the overturning meridional outer flow (see figure 2). The physical mechanism leading to this RW_3 is the instability of the radial swirling jet at $z = 0$ formed by the separation of the cylinder wall boundary layer.

The symmetry-breaking bifurcation leading to RW_3 is a supercritical Hopf bifurcation (of type IV). Figure 21 shows the variation with Re of E_3 for RW_3, indicating that for $\Gamma = 0.25$, the Hopf bifurcation occurs at $Re \approx 1450$. At $Re \approx 2200$, RW_3 undergoes a supercritical Neimark–Sacker bifurcation that introduces an $m = 2$ azimuthal mode, leading to a modulated rotating wave $MRW_{3,2}$.

Much of the dynamics captured by the computations for the extended system with $\Gamma = 0.25$ were also observed in the free-surface experiments. However, the experiments in this case were much more difficult to reproduce than those in the deep system ($\Gamma = 2.0$). Specifically, when nearly perfect experimental conditions were achieved, in terms of water level (initially flat interface) and cleanliness of the container and water, then an $m = 3$ mode rotating wave was observed. At $Re = 2000$, the $m = 3$ wave becomes evident shortly after the base flow is established, and it remains the dominant mode for the duration of the experiments, which lasted up to 2 hours (corresponding to over 3500 rotations of the endwall). Apart from needing nearly perfect initial conditions, the experiments in which the robust $m = 3$ rotating wave were observed also required very low levels of vibration in the laboratory and thus had to be run late in the evening. On the other hand, if lower quality water (with a larger amount of surface-active contaminants) was used, then an $m = 2$ rotating wave was observed shortly after start up, and it persisted.

The results of DPIV measurements showing the axial vorticity of the $m = 3$ rotating wave (together with projected velocity vectors) at $Re = 2000$ are presented in figure 22 (*a*). The structure of the flow at mid-depth ($z = -0.5\Gamma$) is very similar to the computed RW_3 of the extended system, shown in part (*b*) of the figure. This suggests that the mode breaking the axisymmetry in the experiment is the same as that in the

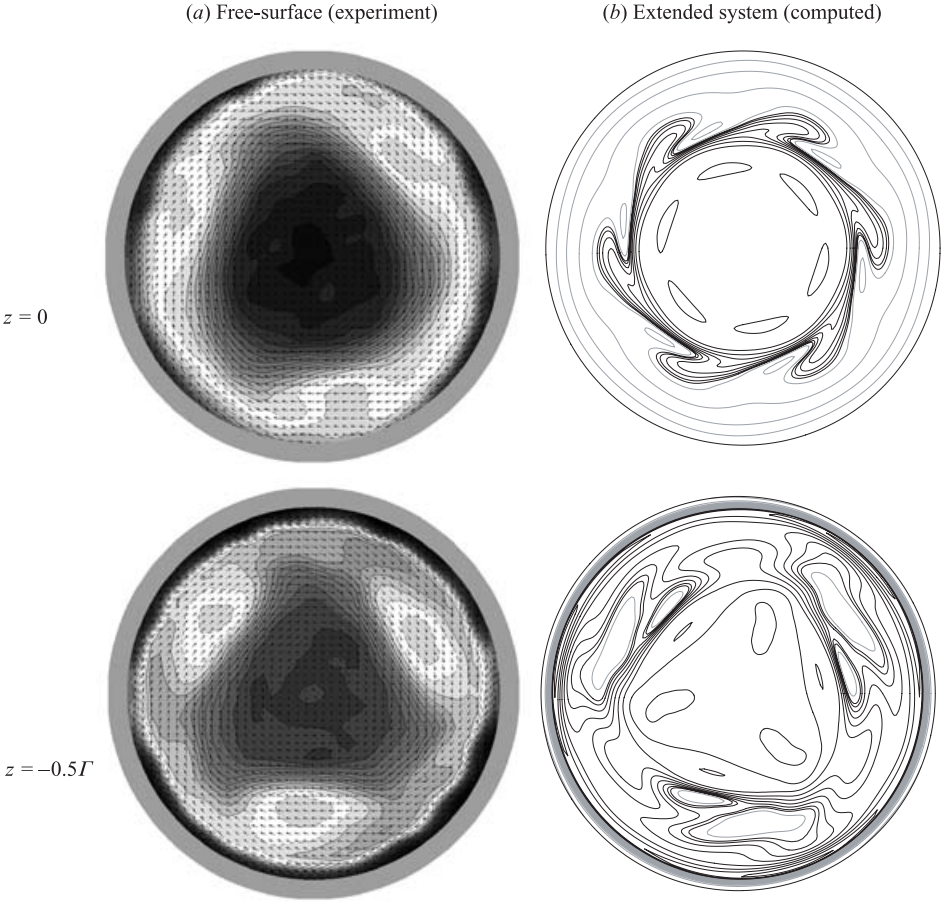

FIGURE 22. Comparison between experimentally measured and computed z-vorticity at the interface ($z=0$) and at mid-depth ($z=-0.5\Gamma$) for RW_3 at $Re=2000$ and $\Gamma=0.25$.

computations. However, the computed RW_3 at $z=0$ is fundamentally different from the measurements at the free surface. The computed mode has odd z-parity, and this mode does not exist in a system with a flat stress-free interface at $z=0$ (we computed it only in the extended system without any imposed conditions at $z=0$). So, that this mode is present in the physical experiment is only possible because the air/water interface is not perfectly flat and stress-free.

The imperfections in the free-surface experiments due to surface-active contaminants and the resultant shear stress at the interface are not easy to quantify, since we had taken all practical steps to minimize contaminants and no surfactants were intentionally added. However, the imperfections due to departures from a flat air/water interface are straightforward to measure, at least in the mean. A laser probe was utilized, where the beam from a He-Ne laser was directed up from the rotating glass bottom endwall and the refraction of the beam was used to determine the local slope of the air/water interface. The distribution of the free-surface slope, averaged in time (which for a rotating wave state is equivalent to averaging in θ), as a function of scaled radial distance from the axis, r, is shown in figure 23(a). Although there is scatter in the data, the general trend is as expected, with essentially zero slope at

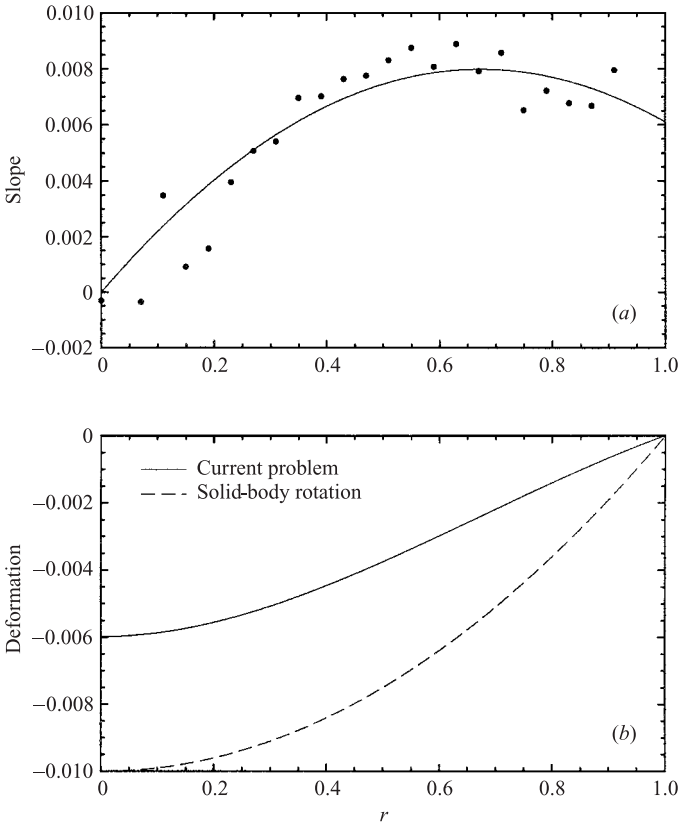

FIGURE 23. (*a*) Measured mean slope of the surface obtained using a laser gauge (filled circles) and a quadratic fit to the data (solid line: slope$(r) = 0.0237r - 0.0176r^2$) for the flow in a shallow system with $\Gamma = 0.26$ at $Re = 2000$ with $Fr = 0.091$. (*b*) Mean deformation of the free surface (scaled by the radius, 25 mm), estimated from the surface slope fit (solid line) with zero deformation at $r = 1$: deformation$(r) = 0.01185r^2 - 0.005867r^3 - 0.00598$, and free-surface deformation for solid-body rotation in a rotating cylinder (Lugt 1996).

the axis. Since the meniscus is effectively pinned at the cylinder wall, $r = 1$ (water wets the wall of the stationary cylinder but not the hydrophilic coated top rim of the cylinder), a finite slope is to be expected at $r = 1$. The surface deformation, computed by integration of the curve fit to the slope data, is presented in figure 23(*b*). Since the interface was initially flat, a deficit in the volume of liquid in the cylinder is apparent from the data. This missing volume of fluid has most likely been transferred to the region between the stationary cylinder at $r = 1$ and the outer (rotating) cylindrical container (see figure 1) through the finite gap (about 0.07 mm) between the stationary cylinder at $r = 1$ and the rotating bottom endwall at $z = -\Gamma$. For comparison, the shape of the interface in the case of solid-body rotation (flow in a rotating cylinder with a free surface, e.g. see Lugt 1996) is also plotted as a dashed line in figure 23(*b*). As expected, the maximum deformation is smaller in the case of a stationary cylinder with a rotating endwall than in the rotating cylinder, due to the secondary meridional flow with inward radial flow at the air/water interface. In the experiments, Fr is small but finite ($Fr = \Omega^2 R^2/gH = 0.091$, where g is the gravitational acceleration), whereas in the computations of the extended system Fr is essentially infinite.

7. Concluding remarks

Modelling this simple free-surface flow in a stationary cylinder, which is driven by the rotation of a bottom endwall, with a flat stress-free interface is fine for the (axisymmetric) basic state because the basic state has even z-parity. As long as the imperfections in the physical system are small, they do not qualitatively affect the flow.

The physical mechanisms responsible for the primary instabilities of the basic state observed in the deep ($\Gamma = 2$) and shallow ($\Gamma = 0.25$) cases are different. In the deep case the instability is due to the jet-like shear layer, formed by the turning of the rotating endwall boundary layer into the interior, becoming unstable. In contrast, for the shallow case the region between the core (in solid-body rotation) and the overturning meridional flow becomes unstable to azimuthal disturbances.

In the deep system ($\Gamma = 2$), the basic state loses stability to a mode with even z-parity, so the imperfections in the physical free-surface experiment do not qualitatively change the dynamics and we find quantitative agreement for the primary symmetry-breaking instability between the experiments and computations with an imposed flat stress-free interface.

In the shallow system ($\Gamma = 0.25$), the primary instability mode has odd z-parity. In the computational model, this mode only exists when odd z-parity is permitted. The flat stress-free boundary condition imposes a hidden symmetry, restricting the solution to an even z-parity subspace. We are able to compute the odd z-parity primary mode in an extended system that does not impose parity conditions. In the experiment, although we attempted to achieve a flat stress-free interface, this is not possible due to imperfections, including Froude number and surfactant Marangoni effects, and so the experiment does not have any z-parity restriction. The basic state spontaneously loses stability to the odd z-parity mode at the critical Re. The computed RW_3 that bifurcates cannot truly represent the physical system because $w \neq 0$ at $z = 0$; but neither can the stress-free model. Due to the presence of imperfections in the experiment (non-flat surface, surfactants and the corresponding stresses), the physical flow does not posses the hidden symmetry implied by the stress-free boundary conditions. Nevertheless, away from $z = 0$, the computed RW_3 resembles strikingly well the observed experimental flow, and captures in detail the complicated structure, so it is a better model than the stress-free model. The differences in this mode between the computations and experiments are in the region near the interface.

We wish to thank Mr J. Leung for making the surface slope measurements. We also thank Dr M. J. Vogel for many useful discussions and assistance with the various measurements and data analysis. This work was partially supported by NSF grants CTS-9908599, CTS-0116947 and CTS-0116995 and (USA), and MCYT grant BFM2001-2350 (Spain).

REFERENCES

Blackburn, H. M. & Lopez, J. M. 2002 Modulated rotating waves in an enclosed swirling flow. *J. Fluid Mech.* **465**, 33–58.

Brons, M., Voigt, L. K. & Sorensen, J. N. 2001 Topology of vortex breakdown bubbles in a cylinder with a rotating bottom and a free surface. *J. Fluid Mech.* **428**, 133–148.

Busse, F. H. & Bolton, E. W. 1984 Instabilities of convection rolls with stress-free boundaries near threshold. *J. Fluid Mech.* **146**, 115–125.

Chandrasekhar, S. 1961 *Hydrodynamic and Hydromagnetic Stability*. Oxford University Press.

Davies, J. T. & Rideal, E. K. 1963 *Interfacial Phenomena*. Academic.

Escudier, M. P. 1984 Observations of the flow produced in a cylindrical container by a rotating endwall. *Exps. Fluids* **2**, 189–196.

Gelfgat, A. Y., Bar-Yoseph, P. Z. & Solan, A. 2001 Three-dimensional instability of axisymmetric flow in a rotating lid-cylinder enclosure. *J. Fluid Mech.* **438**, 363–377.

Goldstein, H. F., Knobloch, E., Mercader, I. & Net, M. 1993 Convection in a rotating cylinder. Part 1. Linear theory for moderate Prandtl numbers. *J. Fluid Mech.* **248**, 583–604.

Handler, R. A., Saylor, J., Leighton, R. I. & Rovelstad, A. L. 1999 Transport of a passive scalar at a shear-free boundary in fully developed turbulent open channel flow. *Phys. Fluids* **11**, 2607–2625.

Hirsa, A. H., Lopez, J. M. & Miraghaie, R. 2001 Measurement and computation of hydrodynamic coupling at an air/water interface in the presence of an insoluble monolayer. *J. Fluid Mech.* **443**, 271–292.

Hirsa, A. H., Lopez, J. M. & Miraghaie, R. 2002*a* Determination of surface shear viscosity via deep-channel flow with inertia. *J. Fluid Mech.* **470**, 135–149.

Hirsa, A. H., Lopez, J. M. & Miraghaie, R. 2002*b* Symmetry breaking to a rotating wave in a lid-driven cylinder with a free surface: Experimental observation. *Phys. Fluids* **14**, L29–L32.

Hunt, J. C. R. 1984 Turbulence structure in thermal convection and shear-free boundary layers. *J. Fluid Mech.* **138**, 161–184.

Iooss, G. & Adelmeyer, M. 1998 *Topics in Bifurcation Theory and Applications*, 2nd edn. World Scientific.

Lamb, J. S. W. & Melbourne, I. 1999 Bifurcation from discrete rotating waves. *Arch. Rat. Mech. Anal.* **149**, 229–270.

Lopez, J. M. 1990 Axisymmetric vortex breakdown: Part 1. Confined swirling flow. *J. Fluid Mech.* **221**, 533–552.

Lopez, J. M. 1995 Unsteady swirling flow in an enclosed cylinder with reflectional symmetry. *Phys. Fluids* **7**, 2700–2714.

Lopez, J. M. & Hirsa, A. 2000 Surfactant influenced gas/liquid interfaces: Nonlinear equation of state and finite surface viscosities. *J. Colloid Interface Sci.* **229**, 575–583.

Lopez, J. M., Marques, F. & Shen, J. 2002 An efficient spectral-projection method for the Navier-Stokes equations in cylindrical geometries II. Three dimensional cases. *J. Comput. Phys.* **176**, 384–401.

Lugt, H. J. 1996 *Introduction to Vortex Theory*. Potomac, Maryland: Vortex Flow Press.

Marques, F. & Lopez, J. M. 2001 Precessing vortex breakdown mode in an enclosed cylinder flow. *Phys. Fluids* **13**, 1679–1682.

Marques, F., Lopez, J. M. & Shen, J. 2002 Mode interactions in an enclosed swirling flow: a double Hopf bifurcation between azimuthal wavenumbers 0 and 2. *J. Fluid Mech.* **455**, 263–281.

Marsden, J. E. & McCracken, M. 1976 *The Hopf Bifurcation and Its Applications*. Springer.

Miraghaie, R. 2002 Experimental investigation of interfacial hydrodynamics of swirling flow in the presence of insoluble monolayers. PhD thesis, Department of Mechanical Engineering, Rensselaer Polytechnic Institute.

Nore, C., Tuckerman, L. S., Daube, O. & Xin, S. 2003 The 1:2 mode interaction in exactly counter-rotating von Karman swirling flow. *J. Fluid Mech.* **477**, 51–88.

Pan, Y. & Banerjee, S. 1995 Numerical study of free-surface turbulence in channel flow. *Phys. Fluids* **7**, 1649–1664.

Scheel, S. & Seehafer, N. 1997 Bifurcation to oscillations in three-dimensional Rayleigh-Bénard convection. *Phys. Rev.* E **56**, 5511–5516.

Schlichting, H. & Kestin, J. 1979 *Boundary-Layer Theory*, 7th edn. McGraw-Hill.

Scott, J. C. 1975 The preparation of water for surface-clean fluid mechanics. *J. Fluid Mech.* **69**, 339–351.

Spohn, A. 1991 Ecoulement et éclatement tourbillonnaires engendrés par un disque tournant dans une enceinte cylindrique. PhD thesis, I'Universite Joseph-Fourier, Grenoble I.

Spohn, A. & Daube, O. 1991 Recirculating flows in a cylindrical tank. In *Computational Methods and Experimental Measurements V. Montreal, 1991* (ed. A. Sousa, C. A. Brebbia & G. M. Carlomagno), pp. 155–166. Elsevier.

Spohn, A., Mory, M. & Hopfinger, E. J. 1993 Observations of vortex breakdown in an open cylindrical container with a rotating bottom. *Exps. Fluids* **14**, 70–77.

Spohn, A., Mory, M. & Hopfinger, E. J. 1998 Experiments on vortex breakdown in a confined flow generated by a rotating disk. *J. Fluid Mech.* **370**, 73–99.

Stevens, J. L., Lopez, J. M. & Cantwell, B. J. 1999 Oscillatory flow states in an enclosed cylinder with a rotating endwall. *J. Fluid Mech* **389**, 101–118.

Teixeira, M. A. C. & Belcher, S. E. 2000 Dissipation of shear-free turbulence near boundaries. *J. Fluid Mech.* **422**, 167–191.

Valentine, D. T. & Jahnke, C. C. 1994 Flows induced in a cylinder with both end walls rotating. *Phys. Fluids* **6**, 2702–2710.

Walker, D. T., Leighton, R. I. & Garza-Rios, L. 1996 Shear-free turbulence near a flat free surface. *J. Fluid Mech.* **320**, 19–51.

Young, D. L., Sheen, H. J. & Hwu, T. Y. 1995 Period-doubling route to chaos for a swirling flow in an open cylindrical container with a rotating-disk. *Exps. Fluids* **18**, 389–392.